Surface structure of nickel oxide layers on a Rh(111) surface

L. Gragnaniello [a,b], F. Allegretti [a,c], R.R. Zhan [d,e], E. Vesselli [d,e], A. Baraldi [d,e], G. Comelli [d,e], S. Surnev [a,*], F.P. Netzer [a]

[a] Institute of Physics, Surface and Interface Physics, Karl-Franzens University Graz A-8010 Graz, Austria
[b] École Polytechnique Fédérale de Lausanne (EPFL), Institut de Physique de la Matière Condensée (IPMC), PH A1 375 (Bâtiment PH) Station 3, CH-1015 Lausanne, Switzerland
[c] Physik Department E20, Technische Universität München, James-Franck Strasse, D-85748 Garching, Germany
[d] Physics Department and Center of Excellence for Nanostructured Materials, University of Trieste, Via Valerio 2, I-34127 Trieste, Italy
[e] IOM-CNR, Laboratorio TASC, AREA Science Park, S.S. 14 Km 163.5, 34149 Trieste, Italy

ARTICLE INFO

ABSTRACT

The formation of nickel oxide nanolayers by oxidizing Ni overlayers on Rh(111) has been investigated and their structures are reported as a function of the nickel coverage and oxygen pressure. Scanning tunneling microscopy (STM), low-energy electron diffraction (LEED), X-ray photoelectron spectroscopy (XPS) and diffraction (XPD), and high-resolution electron energy loss spectroscopy (HREELS) have been applied to characterize the structure and stoichiometry of the nickel oxide nanolayers. Several different phases have been observed depending on the strain state of the metallic Ni overlayers. For the pseudomorphic Ni monolayer, two distinctly different oxide phases with (6×1)-Ni_5O_5 and $(2\sqrt{3} \times 2)$-Ni_8O_{10} structures have been identified at oxygen-poor ($p = 5 \times 10^{-8}$ mbar) and oxygen-rich ($p \geq 1 \times 10^{-6}$ mbar) conditions, respectively. Above one monolayer, where the Ni layers are relaxed, bulk-like NiO(100) films form at the O-rich conditions, whereas chemisorbed-type $p(2 \times 2)O-Ni(111)$ layers develop in the O-poor regime. X-ray photoelectron diffraction analysis has provided additional insight into the relaxation mechanism and the detailed atomic structure of the Ni-oxide nanolayers.

© 2013 Elsevier B.V. All rights reserved.

1. Introduction

The (111)-oriented polar NiO single crystal surfaces and thin films have been intensively investigated, both experimentally and theoretically, aiming at unraveling the polarity compensation mechanism at the atomic level (for an overview, see e.g. [1]). Most of these studies indicate a surface stabilization by an octopolar $p(2 \times 2)$ reconstruction [2–4] or by hydroxylation [5,6]. Yet, the situation for metal-supported Ni-oxide films with a thickness of only few atomic layers, which are often referred to as *oxide nanolayers*, is less clear. Here, additional stabilization mechanisms are possible, such as electrostatic screening by the metallic substrate, interface mechanisms including lattice matching, bond distortions and layer buckling, or the actual ground state of the polar nanolayer may be different from the corresponding bulk counterpart. The progress in the polarity concepts of finite oxide systems has been recently reviewed in a comprehensive article by Goniakowsky et al. [1].

FCC(111) metal surfaces have been typically preferred as substrates for polar oxide films, as their symmetry favors the growth of (111)-oriented NiO films. The key parameter, controlling the structure of the oxide film, is then the mismatch between the metal and NiO(111) surfaces. The low mismatch of 2% has favored the epitaxial

growth of (2×2)-reconstructed NiO(111) films on Au(111) [4], whereas on Cu(111) [7] and Pt(111) [8] surfaces, the higher lattice mismatch (13% and 6%, respectively) precludes the formation of ordered NiO(111)-like structures and instead a more complex phase behavior has been reported, involving the formation of novel oxide structures stabilized at the metal–oxide interface. For example on Pt(111), depending on the oxygen pressure, three different NiO_x structures with (2×2), (7×1) and (4×2) periodicities have been observed in the monolayer coverage regime by STM, but only tentative structure models have been proposed [8].

In the present study, we concentrate on the effects of overlayer strain on the formation of Ni-oxide films and have studied the oxidation of epitaxial Ni layers on a Rh(111) substrate (7.4% lattice mismatch to Ni(111)). We have investigated the surface structure and overlayer chemical nature, by using a combination of scanning tunneling microscopy (STM), low-energy electron diffraction (LEED), X-ray photoelectron diffraction (XPD), X-ray photoelectron electron spectroscopy (XPS) and high-resolution electron energy loss spectroscopy (HREELS) measurements. Depending on the Ni metal overlayer strain, we have encountered two different growth situations for the Ni-oxide nanolayers. The first Ni layer is pseudomorphically strained and this results in the formation of two surface oxide phases with (6×1) and $(2\sqrt{3} \times 2)$ periodicities at oxygen-poor and oxygen-rich conditions, respectively, which exhibit formal Ni_5O_5 and Ni_8O_{10} stoichiometries. 2–5 ML Ni metal overlayers are structurally relaxed and are thus less reactive — they mimic at low oxygen pressures the adsorption behavior of Ni(111) single crystal surfaces, where an atomically smooth (2×2) layer of chemisorbed oxygen

forms. Oxidation of these films at higher oxygen pressures yields bulk-like epitaxial NiO(100) oxide films.

2. Experimental details

Nickel oxide layers with a thickness of up to 5 monolayers (one monolayer (ML) corresponds to the number of surface atoms on the Rh(111) surface) have been prepared by UHV deposition of Ni metal onto a clean Rh(111) surface held at 150 °C, followed by oxidation in a molecular oxygen atmosphere (post-oxidation). The sample temperature during the oxidation was kept at 350 °C for 5 min and the oxygen pressure was varied between 5×10^{-8} mbar and 1×10^{-6} mbar. The Ni deposition rate has been controlled by a quartz microbalance. The STM experiments have been performed in a custom-designed variable-temperature STM system as described previously [9]. All STM images presented here have been recorded at room temperature and in constant-current mode. High-resolution electron energy loss spectroscopy (HREELS) measurements have been performed in a second UHV system [10] with a primary energy of 5.5 eV, in a specular reflection geometry $\Theta_{in} = \Theta_{out} = 60°$, with a typical resolution of 5 meV as measured at the full width at half maximum (FWHM) of the reflected primary peak.

X-ray photoelectron spectroscopy (XPS) and diffraction (XPD) measurements have been carried out in a third UHV system at the Surface Science Laboratory of Elettra-Sincrotrone Trieste using a monochromatised Al K_α radiation ($h\nu = 1486.6$ eV) and a VG MKII hemispherical electron energy analyzer. A five-degree of freedom VG Omniax manipulator is excentrically mounted on a differentially pumped rotary flange, so that different instruments, positioned on the radially distributed flanges, can be reached. The movement system, the instrument controls and the data acquisition are fully computer driven by custom Labview software. The sample crystallographic directions were aligned by means of LEED, which has been used also to control the structure of the nickel oxide films and thus to ensure identical oxide preparation conditions in all three UHV chambers. XPD measurements were acquired with the sample kept at room temperature. Due to the long measuring time required to collect angular scans needed to yield the full hemispheric mapping, cleaning and preparation cycles were regularly alternated with data collection. The photoelectron intensities were obtained by fitting the spectra with Doniach-Šunjić [11] functions, which account for the core-hole lifetime (Lorentzian width) and for the asymmetry of the peaks, convoluted with Gaussians, related to the thermal, inhomogeneous and instrumental broadening. The modulation function, which is defined as $\chi = (I - I_0)/I_0$ [12], was calculated for each angular scan. For the two-dimensional (2D) stereographic projection of the XPD data the intensities were normalized as a function of the polar angles with a cosine function accounting for the angular dependent intensity attenuation.

The XPD simulations have been performed using the MSCD package developed by Chen and Van Hove [13,14]. Non-structural parameters, such as the inner potential and the Debye temperature were obtained from the literature, while the scattering order, cluster size, maximum angular momentum, pathcut, Rehr-Alberts approximation order [15] and analyzer acceptance angle were brought to convergence. The inelastic mean free path was obtained using the Tanuma-Powell-Penn equation [16]. The overall agreement between simulated and experimental modulation functions was quantified by a multispectral reliability factor R, defined as a normalized sum of the square deviations between the calculated and the experimental χ functions: $R = \sum \left(\chi_{exp,i} - \chi_{sim,i} \right)^2 / \sum \left(\chi_{exp,i}^2 + \chi_{sim,i}^2 \right)$ [12]. In order to minimize the R^i-factor a customized approach was adopted, which makes use of both Steepest Descent [17] and genetic algorithms [17–20].

3. Results and discussion

It is instructive to examine first the structure of the metallic Ni films on the Rh(111) surface prior to their oxidation. Fig. 1 shows

STM images taken after the deposition of 0.5 ML (a), 1.0 ML (b) and 1.5 ML Ni (c). The first Ni layer (Fig. 1a,b) exhibits a characteristic network of line protrusions, running along the three equivalent <110> substrate directions, which have been assigned to domain boundaries separating pseudomorphic areas with fcc and hcp stacking [21,22]. This causes a partial strain relief in the first Ni layer (note that the bulk lattice constants of the Rh(111) and Ni(111) surfaces are 2.69 Å and 2.49 Å, respectively, which corresponds to a 8% misfit). The second Ni layer nucleates at the lower step edges and extends into the terrace areas (Fig. 1c). It displays triangular protrusions (inset of Fig. 1c), which are arranged in a hexagonal moiré pattern with a periodicity of 43 Å ± 3 Å. Applying the moiré formula to the latter yields an interatomic distance of 2.5 Å ± 0.2 Å, which (within the error bars) is identical to the bulk Ni(111) lattice constant. This result is also corroborated by the LEED image of 2 ML Ni on Rh(111) in Fig. 1d, which shows hexagons of satellite spots surrounding the main LEED reflexes, in agreement with previous results [23]. The separation between the main and satellite diffraction spots (see inset in Fig. 1d) corresponds to the difference of the reciprocal lattice constants of the Rh(111) and Ni(111) surfaces.

In the following two subsections the evolution of the structure of the Ni-oxide layers with increasing Ni coverage will be presented for two oxygen pressure regimes of the post-oxidation step, which we will refer to as *oxygen-poor* and *oxygen-rich*. At intermediate oxygen pressures mixed and ill-defined oxide phases form, these will not be discussed here.

3.1. Oxygen-poor regime: $p(O_2) = 5 \times 10^{-8}$ mbar

Oxidation of submonolayer Ni coverages at 5×10^{-8} mbar oxygen pressure results in the formation of 2D Ni-oxide islands ($\Theta_{Ni} = 0.5$ ML, Fig. 2a) with a lateral size ranging between 200 Å and 500 Å and an apparent height of 1.7 Å ± 0.2 Å. In the STM images the oxide islands display bright stripes occurring in three domains parallel to the equivalent <110> substrate directions. The atomically-resolved STM image shown in the inset of Fig. 2a reveals that the stripes represent double rows, which are pseudomorphically aligned along the <110> direction and are separated by 6 Rh lattice constants, thus yielding a (6×1) superstructure (unit cell marked on the image). The atomic corrugations along and across the stripes are 0.1 Å and 0.3 Å, respectively. In between the stripes hexagonally ordered flat areas can be spotted. At 1 ML Ni coverage the Rh(111) surface is almost entirely covered by the (6×1) Ni-oxide overlayer (Fig. 2b). A few small clusters are seen on top, which mark the onset of growth of the next layer. The (6×1) superstructure is consistent with the LEED pattern (Fig. 2c), which displays sharp spots with a (6×1) periodicity, thus underlining the good structural order at the long-range scale. Recent density functional theory (DFT) calculations [24] have predicted a model for the (6×1) monolayer phase, which is reproduced in Fig. 2d. It has a formal Ni_5O_5 stoichiometry consisting of a complex configuration of NiO(100)- and NiO(111)-like surface building units, with four-fold (marked by an arrow) and three-fold coordinated oxygen atoms, respectively. The DFT calculations have demonstrated that by means of a particular structural arrangement of these building blocks into a uniaxially reconstructed overlayer a higher thermodynamic stability is achieved with respect to the uniform NiO(100) (non-polar, but highly strained) and NiO(111) (polar) layers [24]. It is noted that a structure with a (7×1) periodicity has been reported recently for Ni-oxide layers on a Pt(111) surface [8], which shows a very similar appearance in the STM images as the (6×1) phase. This structural similarity indicates that the uniaxial (6×1) and (7×1) Ni-oxide phases are not specific for a given oxide–metal interface, but rather derive their stability from polarity cancelation and/or low surface energy effects [24].

The (6×1) phase is only stable up to 1 ML and increasing the Ni coverage transforms into a new structure. The STM image taken after the oxidation of 2 ML Ni on Rh(111) (Fig. 3a) reveals an atomically flat overlayer, which covers almost entirely the surface. Some remnant (6×1) patches can be still seen in the lower- and upper-left parts of the
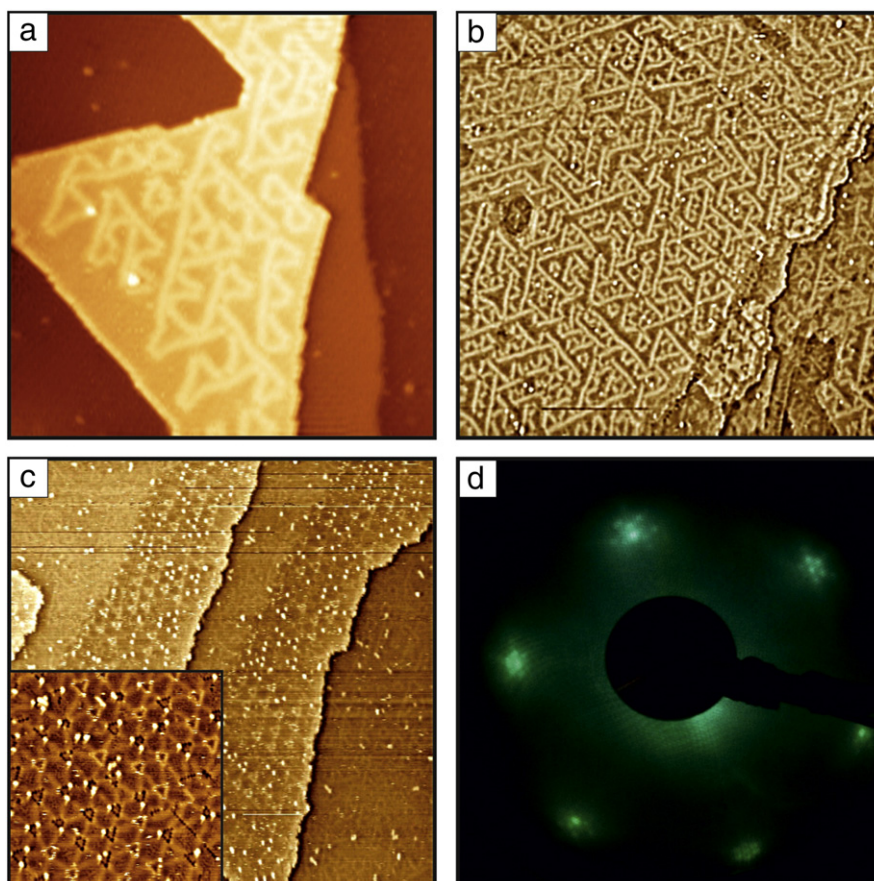
Fig. 1. STM images of Ni overlayers on Rh(111): (a) 0.5 ML–500Å×500Å, 2.0 V, 0.1 nA; (b) 1.0 ML — 1000Å×1000Å, 1.5 V, 0.1 nA; (c) 1.5 ML — 1000Å×1000Å, 1.5 V, 0.1 nA. Inset — 300Å×300Å, 2.0 V, 0.2 nA; (d) LEED pattern (E = 114 eV) of 2 ML Ni on Rh(111).

image, providing a reference plane for measuring the relative apparent height of the second layer, which amounts to ~1.8 Å. The corresponding LEED image (Fig. 3b) exhibits a sharp hexagonal p(2×2) pattern. No structural changes occur upon further increasing the Ni coverage up to 5 ML — STM images (for 3 ML, see Fig. 3c) display large atomically flat terraces as before with the p(2×2) LEED pattern. High-resolution STM images (Fig. 3d) show over a broad range of tunneling resistances a hexagonal lattice (unit cell indicated) of broad protrusions with triangular shape, whose atomic corrugation varies between 0.1 Å and 0.2 Å. At very low tunneling resistance (<1 MΩ) a tripod-like structure can be well resolved (inset of Fig. 3d), which is reminiscent of the STM appearance of the octopolar (2×2)-reconstructed NiO(111) surface [8]. However, careful evaluation of the spacing between the maxima in the STM images in Fig. 3d yields a value of 5.0 Å ± 0.2 Å, which is clearly different from the lattice constant of the (2×2)-NiO(111) surface (5.9 Å). A p(2×2) superstructure of the Rh(111) surface can also be ruled out (5.38 Å), but a p(2×2)-Ni(111) reconstruction with a lattice parameter of 4.98 Å is a very good candidate for the observed structure. It should be considered that the metallic Ni film on Rh(111) adopts from the second layer on approximately the lattice constant of the Ni(111) surface. Since the latter surface exhibits a well-known p(2×2) reconstruction upon adsorption of 1/4 ML oxygen [25,26], we ascribe the structure reported in Fig. 3 to a chemisorbed oxygen phase on a bulk-like Ni(111) layer on Rh(111). This assignment is unambiguously confirmed by HREELS and XPS results, which are presented next.

Fig. 4a shows HREELS spectra taken from the 1 ML $(6×1)$-Ni_5O_5 and 2 ML p(2×2) surfaces. The (6×1) phase exhibits two phonon loss peaks at 51 meV and 60.5 meV, which have been interpreted on the basis of DFT calculations as two dipole-active modes of the out-of-plane vibrations of the outermost oxygen atom (see the side-view Ni_5O_5 model in Fig. 2d) [24]. The p(2×2) 2 ML phase shows a single loss

peak at 65 meV, which shifts gradually to 69 meV when the Ni coverage increases to 10 ML. The latter phonon loss value is fully compatible with the stretching frequency of oxygen atoms chemisorbed in the three-fold hollow sites on Ni(111) crystal surfaces of 72 meV [27]. In Fig. 4b Ni $2p_{3/2}$ XPS spectra taken from 2 ML Ni on Rh(111) (bottom curve) and after oxidation at $5×10^{-8}$ mbar oxygen (top curve), generating the p(2×2) structure, are shown. For comparison, the corresponding spectrum from the $(6×1)$-Ni_5O_5 monolayer is displayed in the middle. The Ni $2p_{3/2}$ spectrum of the Ni film contains a main emission line with a binding energy of 852.8 eV and a satellite peak shifted by about +6 eV, which is due to a two hole $c^{-1}3d^9 4s^2$ (c^{-1} is a core hole) final state effect [28]. This shape of the Ni 2p spectrum is maintained for the p(2×2) phase — only a small positive shift (+0.2 eV) can be recognized, as expected for chemisorbed oxygen species. A similar chemical shift is observed in the Ni 2p spectrum of the $(6×1)$-Ni_5O_5 monolayer surface, but the 6 eV satellite peak is clearly missing, in accord with the oxidic nature of this phase. Both the peak position and spectral shape of the $(6×1)$-Ni_5O_5 structure are distinctly different from those of the bulk-type NiO phase (see e.g. Fig. 7a), which we attribute to the interfacial bonding and the proximity of the underlying metal surface. The latter may strongly modify both the initial and final states in the photoemission process.

In order to obtain further structural details on the structure of the p(2×2)O phase we collected a set of XPD data for the Ni2p$_{3/2}$ core levels of a 5 ML p(2×2)O – Ni(111) film, as shown in Fig. 5a. The main characteristics of the stereographic plot are the forward scattering spots at about 40° polar angle with a three-fold azimuthal symmetry. To take into account the lattice mismatch between Ni and Rh, we have approximated the structure with a (13×13)-Ni(111) unit cell with 5 Ni layers and 4 bulk Rh layers formed by (12×12)-Rh(111) unit cells, for a total of 845 Ni atoms, 36 O atoms, and 576 Rh substrate atoms. In the structural model yielding the best R-factor (0.23), shown in Fig. 5c, the
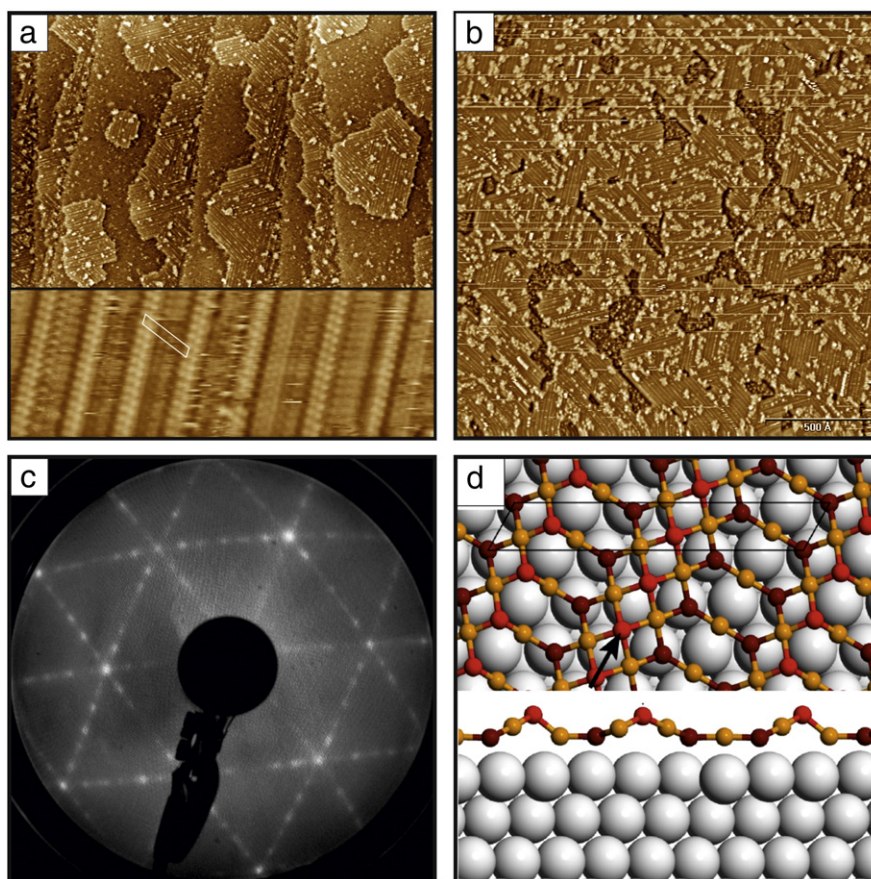
Fig. 2. Large-scale STM images (2000Å×2000Å, 1.0 V, 0.2 nA) of (a) 0.5 ML and (b) 1.0 ML (6×1)-Ni-oxide layers on Rh(111). The inset in panel (a) (110Å×40Å, 15 mV, 2.0 nA) is a high-resolution STM image of the (6×1) phase; (c) LEED pattern (E=150 eV) of the (6×1) phase at 1.0 ML; (d) DFT models (top and side views) of the (6×1)-Ni$_5$O$_5$ structure. Adapted from Ref. [6].

terminal Ni layer displays a buckled displacement (0.23 ± 0.15 Å) of the Ni atoms coordinated to oxygen, which occupies the three-fold hollow site. The structural relaxation was carried out by taking into account all the interlayer distances of the Ni film ($d_{Nin–Nin+1}$ in Fig. 5) and the lattice constants of the intermediate Ni ad-layers (a_{Ni2}, a_{Ni3}, a_{Ni4}). We found a significant compression of the top three layers ($d_{N1–Ni2}$ = 1.70 ± 0.20 Å, $d_{N2–Ni3}$ = 1.70 ± 0.20 Å, $d_{N3–Ni4}$ = 1.80 ± 0.30 Å) in comparison with the interlayer distance of the Ni(111) bulk phase (2.01 Å), even considering the quite large error bars reflecting our moderate sensitivity to the vertical positions of these Ni layers. By contrast, thanks to the large atomic clusters used in our simulations, we are very sensitive to variations of the in-plane lattice parameter of the Ni film which is exponentially reduced in going from the interface region to the film surface. In order to cross-check the correctness of our results, a quantitative comparison between the exponential decay mode and two other possible strain relaxation models are reported in Fig. 5b. In the first case (blue markers) the lattice parameter was varied linearly from 2.69 Å (bottom layer) to 2.49 Å (topmost layer), resulting in an R-factor of 0.56 (For interpretation of the references to color in this figure legend, the reader is referred to the web version of this article.). In the other case, the black-dotted curve, labeled "constant" (black markers), describes a 5 ML thick Ni film, for which the same lattice parameter of 2.46 Å is constrained in all layers, except for the interface layer, which has the same lattice constant of Rh(111) (R-factor 0.46). These results clearly favor the exponential relaxation model, whereas both the constant and the linear relaxation models can be ruled out due to their much larger R-factors.

The question arises, why the chemical bonding and state of oxygen to nickel in the oxygen-poor regime changes from an oxide-type in the (6×1)-Ni$_5$O$_5$ structure to a much weaker chemisorbed-like in the p(2×2)O–Ni phase, when the Ni coverage increases beyond one

monolayer? We attribute this oxidation behavior to the different strained state of the Ni atoms in the first and in the subsequent layers. As established above, the first Ni layer is subject to a tensile stress, which is only partially relieved by the formation of dislocation lines, whereas the second and the following layers become relaxed, with their lattice parameters converging exponentially to the bulk Ni(111) value. As a consequence, an increased reactivity towards oxygen can be expected for the Ni monolayer with respect to the next layers, which is due to the shift of the d-band center towards the Fermi-level predicted for pseudomorphic overlayers with a tensile stress [29,30]. Such a shift of the Ni 3d band has indeed been observed for Ni layers grown onto vicinal Rh(111) surfaces [31]. We have recently shown that 1-D Ni nanowires exhibit also a similarly enhanced oxidation reactivity, due to their strong electronic and elastic coupling to the step atoms of a Rh(553) surface [32].

3.2. Oxygen-rich regime: 2×10^{-7} mbar ≤ $p(O_2)$ ≤ 1×10^{-6} mbar

Dramatic structural changes occur upon oxidation of Ni-films under oxygen-rich conditions. At 1 ML the (6×1) phase is replaced by a rectangular (2√3×2), or alternatively (4×2) superstructure, which exhibits a two-dimensional morphology in the STM images (Fig. 6a). The corresponding LEED pattern (Fig. 6b) displays at all electron energies extinction of odd-numbered superstructure reflections, which implies the presence of glide plane symmetry. High-resolution STM images show a strong bias dependence — images taken at a positive bias voltage U ≤ 0.3 V (Fig. 6c) reveal a pattern of zig-zag protrusions, enclosing an angle of 90°, whereas at U ≥ + 0.6 V (Fig. 6d), only large bright maxima, slightly elongated along the directions of the zig-zag chains, can be discerned. Both the rectangular (2√3×2) and (4×2) unit cells, together

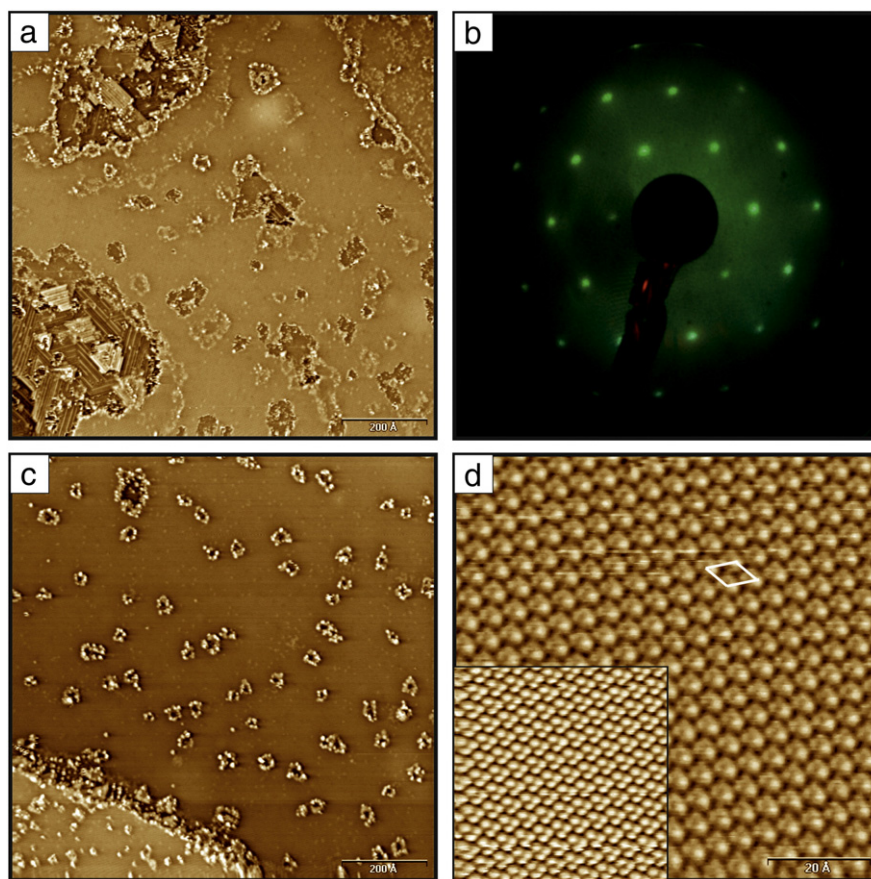**Fig. 3.** Large-scale STM images (1000Å×1000Å, 1.0 V, 0.1 nA) of (a) 2.0 ML and (c) 3.0 ML p(2×2) Ni−O layers on Rh(111); (b) LEED pattern (E=110 eV) of the p(2×2) phase at 2.0 ML; (d) high-resolution STM images (100Å×100Å, 10 mV, 2.0 nA) of the p(2×2) phase (inset − 50Å×50Å, 5 mV, 8.0 nA).

with three glide planes (dashed lines), are indicated in Fig. 6c. We note that a (4×2) superstructure with a very similar STM appearance has also been reported recently by Hagendorf et al. for a Ni-oxide monolayer
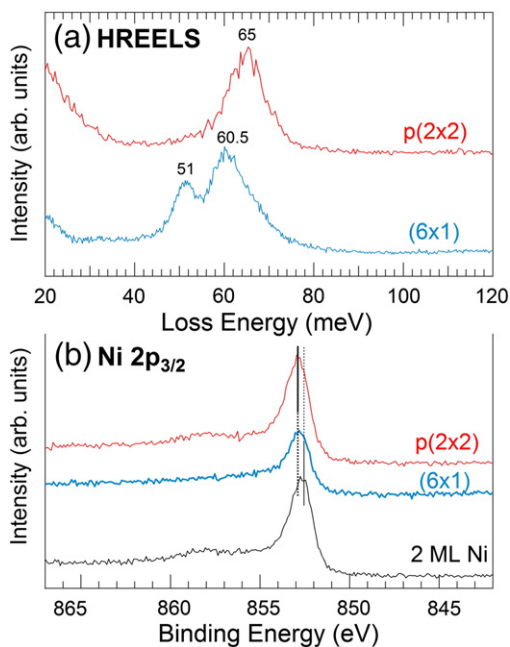

Fig. 4. (a) HREELS phonon loss spectra of the (6×1)-Ni_5O_5 and p(2×2) Ni−O structures at 1.0 ML and 2.0 ML, respectively; (b) XPS Ni $2p_{3/2}$ spectra of the (6×1)-Ni_5O_5 and p(2×2) Ni−O structures. The XPS spectrum of the 2.0 ML Ni/Rh(111) surface is shown for comparison.

on Pt(111) [8]. A two-dimensional ($\sqrt{3}$×2) structure has been observed in STM during the decomposition of NiO(111) thin films on Ni(111) [6], which looks very similar to that shown in Fig. 6d, but with a twice smaller unit cell. We suspect that due to the poor resolution in the latter STM images, the subtle difference in the image contrast between a (2$\sqrt{3}$×2) and a ($\sqrt{3}$×2) unit cell could not be resolved, which may thus have been incorrectly assigned. Kitakatsu et al. have interpreted this structure as residual bulk NiO rows, aligned along the substrate <11$\bar{2}$> directions [6]. These findings suggest that the (2$\sqrt{3}$×2) monolayer can be considered as an intermediate phase between an interface-stabilized oxide layer, whose structure is typically strongly substrate dependent, and a bulk oxide. This is supported by the XPS and HREELS results, as presented next.

Fig. 7 shows XPS Ni $2p_{3/2}$ (a) and O 1s (b) core-level spectra of the (2$\sqrt{3}$ × 2) phase. The Ni $2p_{3/2}$ spectrum has been deconvoluted into three different core-level components with binding energies (BE) of 854.3 eV, 855.4 eV and 861.3 eV, which are characteristic of bulk NiO [33]. More specifically, the lowest BE main line has been assigned to a $c^{-1}3d^9L^{-1}$ final state, where c^{-1} and L^{-1} refer to a hole in the 2p core level and the ligand band, respectively, whereas the shoulder at 855.4 eV has been ascribed to a non-local screening process from neighboring NiO_6 units [34] and/or surface effects [35]. The remaining emission structure at 861.3 eV is a *charge-transfer satellite* (indicated S in Fig. 7a), corresponding to a $c^{-1}3d^8L^{-2}$ final state [33]. This similarity suggests that the Ni atoms have a similar environment as in bulk NiO crystals, i.e. they are coordinated to O atoms only, and are thus not in direct contact with the underlying metal substrate − in the opposite case significant negative core-level shifts may occur as a result of the metal–metal bonding at the substrate–oxide interface [36]. This is also reinforced by the shape of the O 1s spectrum (Fig. 7b), which contains two core-level components with BE of 531.2 eV (marked I) and 529.5 eV (marked II),
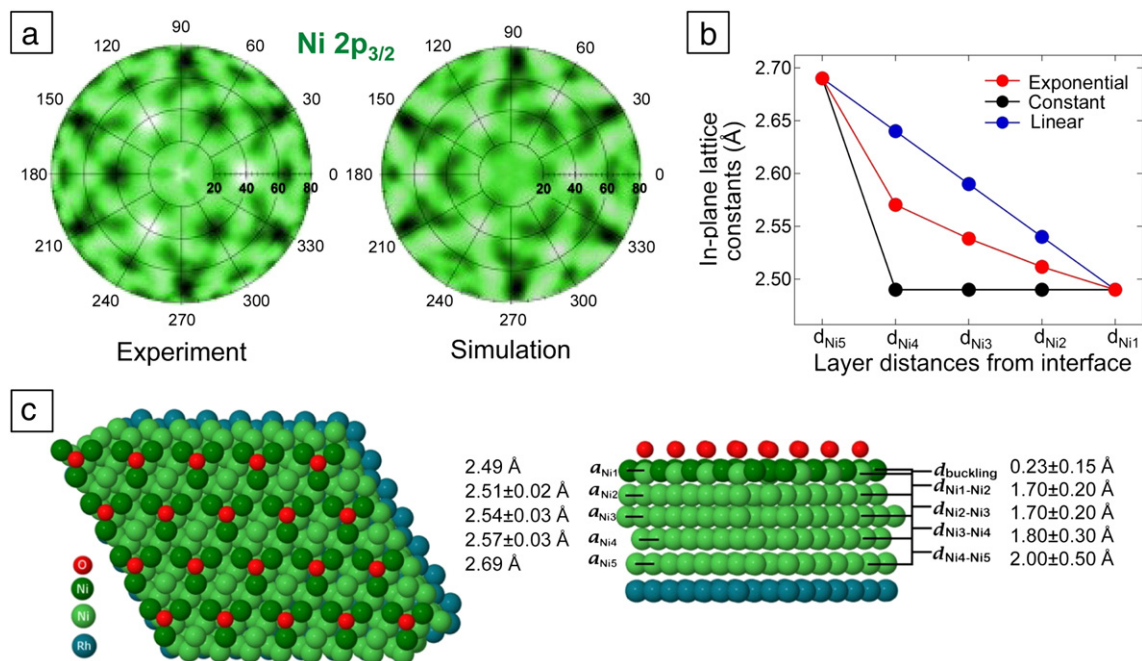
Fig. 5. (a) Experimental (left) and simulated (right) XPD pattern of the Ni $2p_{3/2}$ core levels for the 5 ML p(2×2)-Ni–O chemisorbed phase. (b) In-plane Ni lattice constant behavior for the different strain relaxation models (see text). (c) Top and side view of the lowest R-factor structural model for the 5 ML p(2×2) phase.

implying two geometrically non-equivalent O species. Since there is a transfer of intensity from peak II to peak I in going from normal emission to grazing emission geometry (not shown), we attribute these peaks as due to O atoms located at the oxide–vacuum (I) and substrate–oxide (II) interface, respectively. This assignment is also corroborated by the observation that the two O 1s components show distinctly different XPD
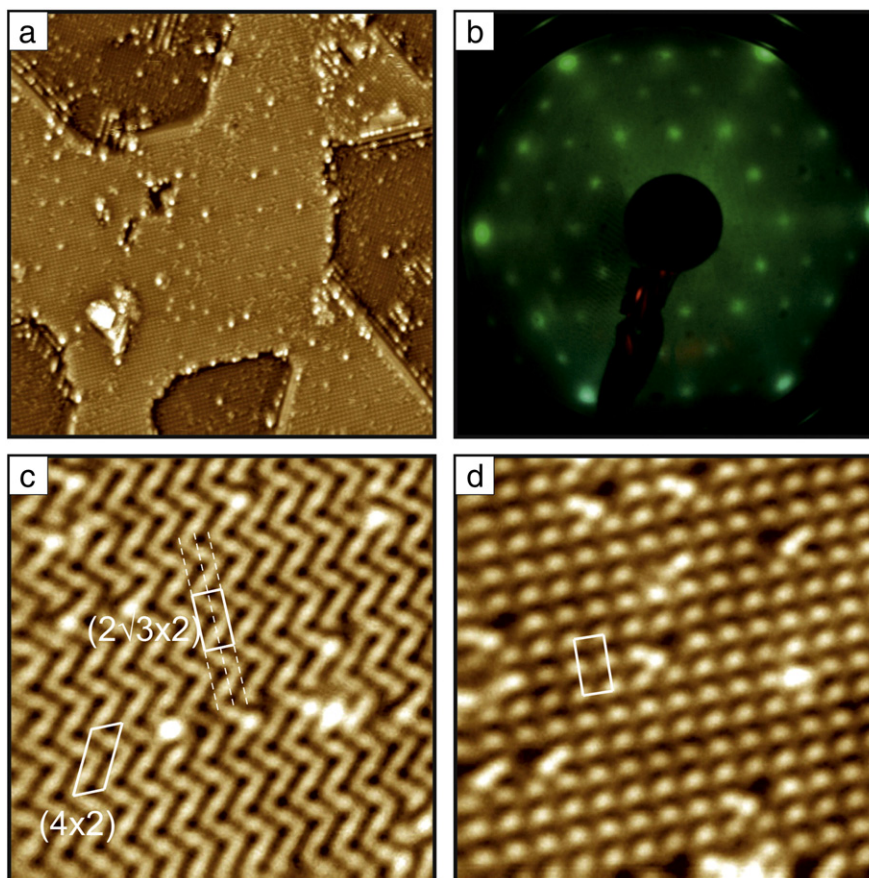

Fig. 6. (a) Large-scale STM image (500Å×500Å, 0.8 V, 0.05 nA) and (b) LEED pattern (E = 65 eV) of the (2√3×2) structure at 1.0 ML. High-resolution STM images (70Å×70Å) of the (2√3×2) phase, taken at bias voltages of 0.3 V (c) and 0.6 V (d). The (4×2) and (2√3×2) unit cells are indicated on the images. The dotted lines indicate the gliding planes, leading to the extinction of some LEED spots.

patterns: while peak II displays a complex hexagonal pattern of forward scattering maxima (see Fig. 8a, top right), which are due to scatterers in well-defined positions above the interface layer, peak I shows no modulation in XPD, as expected for O atoms located above all other scatterers. The overall O coverage in the $(2\sqrt{3}\times2)$ monolayer has been estimated to about 0.75 ML by comparing the O 1s integrated intensity to that of the chemisorbed oxygen p(2×2) phase (corresponding to 0.25 ML) at 5 ML Ni coverage. Finally, the HREELS spectrum of the $(2\sqrt{3}\times2)$ phase, presented in Fig. 9, provides additional evidence that the local bonding in this oxide structure is similar to that in bulk NiO: it contains two phonon losses at 56 meV and 68 meV, which are very close to the values of 54 meV and 69 meV, observed for the bulk-like NiO films.

Based on this information we have constructed a trial structure model of the $(2\sqrt{3}\times2)$ phase, which has been optimized in the XPD analysis. The simulated XPD patterns of both the O1s core level associated with the interface O layer (peak II) and of the Ni 2p$_{3/2}$ core level signal are reported together with the corresponding experimental data in Fig. 8a. The best R-factor (0.21) model is depicted in Fig. 8b and consists of a O–Ni–O trilayer, which is formed by a hexagonally close packed Ni layer (with 8 atoms per $(2\sqrt{3}\times2)$ unit cell), bonded to 6 and 4 oxygen atoms at the interface and surface, respectively. The formal stoichiometry of this trilayer structure is thus Ni_8O_{10}, which is compatible with the experimental Ni (1 ML) and O (1.25 ML) coverages. The interface oxygen atoms occupy threefold-hollow sites at the Rh(111) surface, whereas the terminal O species are found in alternate three-fold (A) and pseudo-bridge (B) sites of the Ni layer (Fig. 8b). The Ni layer results to be not coplanar, with a maximum variation in the atomic position along the surface normal of 0.2 Å. Most importantly, the resulting structure shows a strong buckling of the two non-equivalent first-layer O atoms (0.63 Å), as observed in the side view of Fig. 8b. The Ni–O bond lengths obtained from our XPD analysis range from 1.78 (hollow) to 2.48 Å (quasi-bridge), which match the Ni–O distances commonly found in literature for various Ni–O based compounds (1.78–2.55 Å).

Oxidation of Ni films with coverage between 2 and 3 ML in the 5×10^{-7}–2×10^{-6} mbar oxygen pressure range results in the formation of epitaxial NiO(100) oxide layers with typically rough morphologies, as depicted in Fig. 9a. Atomically-resolved images (inset of Fig. 9a) reveal a square structure with a lattice constant of 2.8 Å ± 0.1 Å, i.e. close to that of the NiO(100) surface (2.95 Å). Since empty states have been probed, we attribute the protrusions in the image to the positions of the Ni ions [37]. The LEED image in Fig. 9b displays along with the Rh substrate spots two concentric rings of 12 diffraction spots each, which are due to three equivalent rotational domains of the NiO(100) layer lattice. The oxide diffraction spots are slightly azimuthally elongated, which is due to a small (~1°) misalignment of the oxide lattice with respect to the Rh(111) surface. The NiO stoichiometry has been confirmed by HREELS:

Fig. 8. (a) Two-dimensional stereographic projections of the Ni 2p$_{3/2}$ and O 1s modulation functions obtained from the experimental XPD spectra of the $(2\sqrt{3}\times2)$ monolayer phase (top) to be compared with the simulated data (bottom) from the relaxed structure; (b) top and side perspective views of the lowest R-factor structural model, corresponding to the simulated plots reported in the upper panel.
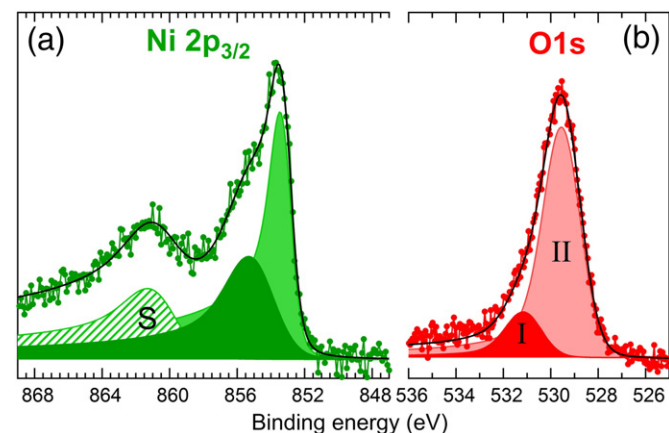

Fig. 7. (a) XPS Ni 2p$_{3/2}$ and (b) O 1s core-level spectra of the $(2\sqrt{3}\times2)$ monolayer phase. Both XPS spectra have been deconvoluted into individual core-level components, as discussed in the text.
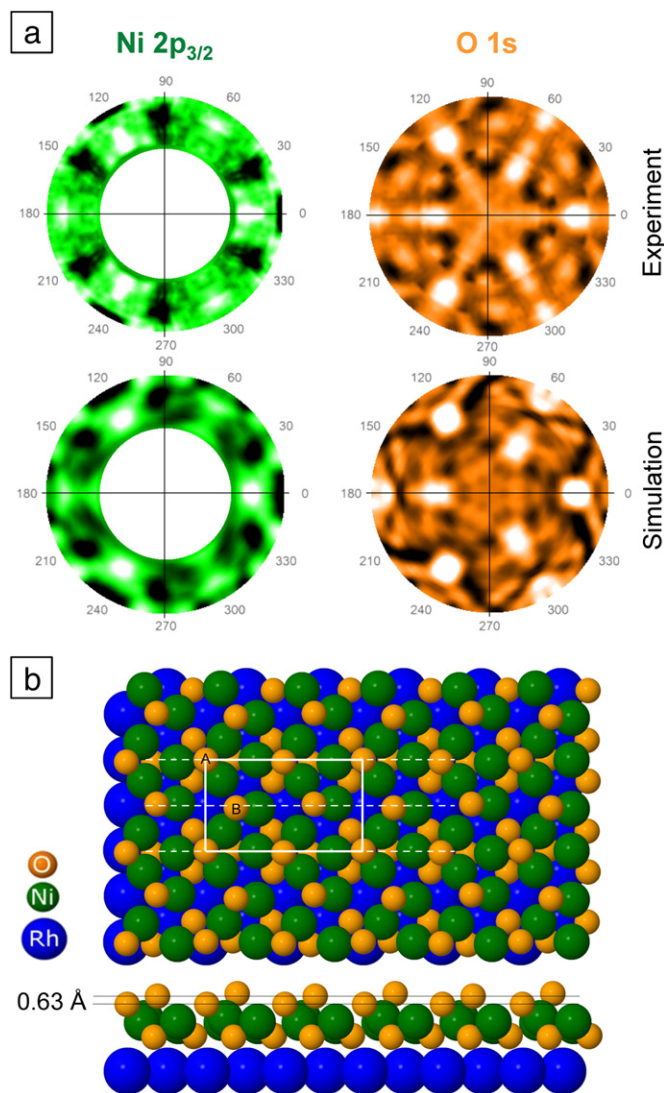
the top spectrum in Fig. 9c, taken from the 2 ML NiO surface, contains a phonon loss peak at 68 meV, which is identified as a Fuchs-Kliewer surface phonon involving ionic displacements normal to the NiO(100) crystal surface [38]. The low-energy shoulder at 54 meV has been also reported in HREELS spectra of NiO films on Ni(100) [39] and Pd(100) [40] surfaces. Interestingly, under a somewhat lower oxygen pressure of 1×10^{-7} mbar, the NiO(100) phase transforms into a surface which exhibits a sharp p(2×2) LEED pattern (not shown), corresponding to a lattice constant of about 5 Å. This surface exhibits a phonon loss feature at 45 meV (bottom spectrum of Fig.9c), which clearly distinguishes it from the chemisorbed p(2×2)-O–Ni(111) structure, mentioned above (the weak intensity around 68 meV is due to some remnant NiO(100)). Although the atomic structure of this phase is not yet clear, we tentatively ascribe the 45 meV phonon loss to oxygen species incorporated into the Ni film, thus in an oxidic-like environment. A further argument in favor of this assignment is the different adsorption behavior of these two p(2×2) surfaces: whereas CO molecules from the UHV background atmosphere readily coadsorb on the chemisorbed O phase (as identified by the presence of characteristic CO stretching vibrations in HREELS) [41], no CO adsorption takes place on the p(2 x 2)-NiOx surface at room temperature. We note, in passing, that the latter structure is also
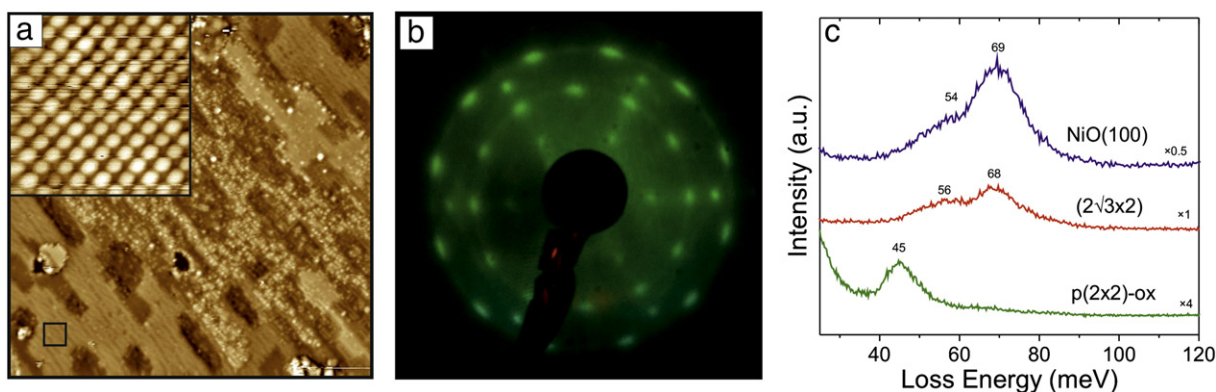
Fig. 9. (a) Large-scale STM image (500Å×500Å, 1.5 V, 0.05 nA) of the NiO(100) surface at 2 ML. The inset (30Å×30Å, 0.1 V, 0.3 nA) is a high-resolution image of the marked square area in (a); (b) corresponding LEED pattern (E = 94 eV); (c) HREELS spectra of the NiO(100) 2 ML film, (2√3×2) monolayer phase and a p(2×2)-oxide surface obtained after post-oxidation of 2 ML Ni film at 1×10^{-7} mbar oxygen.

different from the octopolar-reconstructed (2×2)-NiO(111) phase [4], which has a larger lattice constant of 5.9 Å.

At higher (>3 ML) Ni coverages NiO(111) films with a poor structural order form. In addition, NiO(100) side facets are observed, as revealed by the characteristic streaks in the LEED images. Similar (100) faceting has been recently also observed for NiO films on $Al_2O_3(0001)$ [42] and MnO films on Pd(100) [43] surfaces, which is most likely driven by the lowest surface energy of the non-polar (100) surface of rock-salt oxides.

4. Summary

Ordered nanolayers of NiOx have been grown on a Rh(111) substrate by post-oxidation of Ni films and analyzed as a function of layer thickness and oxygen pressure by STM, LEED, XPS, HREELS and XPD measurements. Up to the first oxide monolayer, two different oxide structures have been detected to form well-defined wetting layers on the Rh(111) surface, with (6×1) and (2√3×2) surface structures that are associated with Ni_5O_5 and Ni_8O_{10} phases, respectively. Above one monolayer and at oxygen-poor conditions a p(2×2) structure forms, which has been identified as chemisorbed oxygen on Ni(111)-like layers. It has been argued that the reason for the enhanced oxidation reactivity at the interface is the tensile stress in the first pseudomorphic Ni layer caused by the 7.4% lattice mismatch. Under oxygen-rich conditions the NiOx films converge to bulk-like NiO(100) phases.

Acknowledgments

References

[1] J. Goniakowsky, F. Finocchi, C. Noguera, Rep. Prog. Phys. 71 (2008) 016501.
[2] A. Barbier, G. Renaud, Surf. Sci. 392 (1997) L15.
[3] A. Barbier, G. Renaud, C. Mocuta, A. Stierle, Surf. Sci. 433–435 (1999) 761.
[4] C.A. Ventrice Jr., Th. Bertrams, H. Hannemann, A. Brodde, H. Neddermeyer, Phys. Rev. B 49 (1994) 5773.
[5] F. Rohr, K. Wirth, J. Libuda, D. Cappus, M. Bäumer, H.J. Freund, Surf. Sci. 315 (1994) L977.
[6] N. Kitakatsu, V. Maurice, P. Marcus, Surf. Sci. 411 (1998) 215.
[7] S. Stanescu, C. Boeglin, A. Barbier, J.-P. Deville, Surf. Sci. 549 (2004) 172.
[8] Ch. Hagendorf, R. Shantyr, H. Neddermeyer, W. Widdra, Phys. Chem. Chem. Phys. 8 (2006) 1575.
[9] S. Surnev, L. Vitali, M.G. Ramsey, F.P. Netzer, G. Kresse, J. Hafner, J. Phys. Rev. B 61 (2000) 13945.
[10] I. Kardinal, M.G. Ramsey, F.P. Netzer, Surf. Sci. 376 (1997) 229.
[11] S. Doniach, M. Sunjic, J. Phys. C: Solid State Phys. 3 (1970) 285.
[12] D.P. Woodruff, Surf. Sci. Rep. 62 (2007) 1.
[13] Y. Chen, et al., Phys. Rev. B 58 (1998) 13121.
[14] Y. Chen, M.A. Van Hove, http://www.ap.cityu.edu.hk/personal-website/Van-Hove_files/mscd/mscdpack.html.
[15] J.J. Rehr, R.C. Albers, Phys. Rev. B 41 (1990) 8139.
[16] S. Tanuma, C.J. Powell, D.R. Penn, Surf. Interface Anal. 17 (1991) 911.
[17] R. Döll, M.A. Van Hove, Surf. Sci. 355 (1996) L393.
[18] M.L. Viana, R. Díez Muiño, E.A. Soares, M.A. Van Hove, V.E. de Carvalho, J. Phys. Condens. Matter 19 (2007) 446002.
[19] M.L. Viana, W. Simões e Silva, E.A. Soares, V.E. de Carvalho, C.M.C. de Castilho, M.A. Van Hove, Surf. Sci. 602 (2008) 3395.
[20] D.A. Duncan, J.I.J. Choi, D.P. Woodruff, Surf. Sci. 606 (2012) 278.
[21] C. Günther, J. Vrijmoeth, R.Q. Hwang, R.J. Behm, Phys. Rev. Lett. 74 (1995) 754.
[22] J.A. Meyer, P. Schmid, R.J. Behm, Phys. Rev. Lett. 74 (1995) 3864.
[23] A. Wander, C.J. Barnes, L.D. Mapledoram, D.A. King, Surf. Sci. 281 (1993) 42.
[24] T. Franz, J. Zabloudil, F. Mittendorfer, L. Gragnaniello, G. Parteder, F. Allegretti, S. Surnev, F.P. Netzer, J. Phys. Chem. Lett. 3 (2012) 186.
[25] A.R. Kortan, R.L. Park, Phys. Rev. B 23 (1981) 6340.
[26] E. Schmidtke, C. Schwennicke, H. Pfnür, Surf. Sci. 312 (1994) 301.
[27] H. Ibach, D. Bruchmann, Phys. Rev. Lett. 44 (1980) 36.
[28] S. Hufner, Photoelectron spectroscopy, Solid State Science Series, vol. 82, Springer-Verlag, 1995.
[29] M. Mavrikakis, B. Hammer, J.K. Nørskov, Phys. Rev. Lett. 81 (1998) 2819.
[30] B. Hammer, J.K. Norskov, in: B.C. Gates, H. Knoezinger (Eds.), Advances in Catalysis, vol. 45, Academic Press, San Diego, 2000, p. 71.
[31] Georg Parteder, Ph.D. Thesis, University of Graz (2009).
[32] J. Schoiswohl, F. Mittendorfer, S. Surnev, M.G. Ramsey, J.N. Andersen, F.P. Netzer, Phys. Rev. Lett. 97 (2006) 126102.
[33] M.A. van Veenendaal, G.A. Sawatzky, Phys. Rev. Lett. 70 (1993) 2459.
[34] D. Adlers, F.C. Voogt, T. Hibma, G. Sawatzky, Phys. Rev. B54 (1996) 7716.
[35] I. Preda, A. Gutiérrez, M. Abbate, F. Yubero, J. Méndez, L. Alvarez, L. Soriano, Phys. Rev. B77 (2008) 075411.
[36] F.P. Netzer, Surf. Rev. Lett. 9 (2002) 1553.
[37] W. Steurer, F. Allegretti, S. Surnev, G. Barcaro, L. Sementa, A. Fortunelli, F.P. Netzer, Phys. Rev. B84 (2011) 115446.
[38] P.A. Cox, A.A. Williams, Surf. Sci. 152 (153) (1985) 791.
[39] J.G. Chen, M.D. Weisel, R.B. Hall, Surf. Sci. 250 (1991) 159.
[40] J. Schoiswohl, S. Agmoli, B. Xu, S. Surnev, M. Sambi, M.G. Ramsey, G. Granozzi, F.P. Netzer, Surf. Sci. 599 (2005) 1.
[41] G. Chiarello, A. Cupolillo, C. Giallombardo, R.G. Agostino, V. Formoso, D. Pacilè, L. Papagno, E. Colavita, Surf. Sci. 536 (2003) 33.
[42] C. Mocuta, A. Barbier, G. Renaud, Y. Samson, M. Noblet, J. Magn. Magn. Mater. 311 (2000) 283.
[43] F. Allegretti, C. Franchini, V. Bayer, M. Leitner, G. Parteder, B. Xu, A. Fleming, M.G. Ramsey, R. Podloucky, S. Surnev, F.P. Netzer, Phys. Rev. B 75 (2007) 224120.